Electronic Research Archive

https://www.aimspress.com/journal/era

ERA, 34(10): 7480–7499.
DOI: 10.3934/era.2026323
Received: 02 June 2026
Revised: 23 August 2026
Accepted: 24 August 2026
Published: 28 August 2026

Research article

Turing bifurcation and linear Hopf threshold in a diffusive predator–prey model with Smith growth and ratio-dependent Holling type III functional response

Jiahong Li[1], Wenjie Li[2,*], Wanqin Wu[1], Xuewen Tan[1,*] and Xinzhi Liu[3]

[1] School of Mathematics and Computer Science, Yunnan Minzu University, Yunnan 650500, China

[2] Department of Mathematics, Kunming University of Science and Technology, Yunnan 650500, China

[3] Department of Applied Mathematics, University of Waterloo, Waterloo N2L 3G1, Canada

* **Correspondence:** Email: wenjieli@kust.edu.cn, tanxw0910@ymu.edu.cn.

Abstract: This paper studies a diffusive predator–prey model with Smith growth, a ratio-dependent Holling type III functional response, and Leslie–Gower predator dynamics. By analyzing the characteristic equations, we derive conditions for Turing instability and a linear stability threshold that signals the onset of Hopf-type oscillations. For the Turing branch, we prove the local existence of non-constant steady states bifurcating from the positive equilibrium, treating simple cases using the Crandall–Rabinowitz theorem. Numerical simulations are then carried out to illustrate these theoretical results and to explore the system's behavior near the intersection of the Turing and Hopf curves, where long-lived transient spatial patterns, spatially inhomogeneous periodic solutions, and complex spatio-temporal oscillatory patterns are observed. Overall, this work offers a mathematical account of how nonlinear growth, ratio-dependent predation, and spatial diffusion together shape the dynamics of this predator–prey system.

Keywords: Turing bifurcation; linear Hopf threshold; diffusive predator–prey model; ratio-dependent Holling type III functional response; Smith growth

1. Introduction

In the study of predator–prey biological models, the combination of the ratio-dependent Holling type III functional response and Smith growth has significant ecological importance. The Holling type III functional response accounts for the nonlinear characteristics of predator efficiency varying with prey density, exhibiting a saturation effect at high prey densities. The ratio-dependent form

incorporates the influence of the predator–prey ratio, more faithfully representing resource competition and predator–prey behavior in natural systems. Smith growth describes the growth dynamics of the prey under resource constraints, and its density-dependent characteristics better capture the effect of environmental carrying capacity on population growth.

Unlike previous studies that separately considered Smith growth [1, 2] or ratio-dependent functional responses [3], the present work combines Smith growth, a ratio-dependent Holling type III functional response, and Leslie–Gower predator dynamics [4]. This combination leads to a reaction–diffusion system whose mathematical structure differs from closely related models in several respects. For instance, while [5] considered a diffusive predator–prey model that incorporates Smith growth, it employs a functional response based on schooling behavior rather than the ratio-dependent Holling type III formulation used here; this structural difference fundamentally alters the density dependence and the resulting Turing bifurcation curves. [6] considered a modified Leslie–Gower system with Smith growth, yet employs a nonmonotonic functional response rather than the ratio-dependent Holling type III used here; this difference significantly affects the spectral conditions and the shape of the Hopf boundary. [7] incorporated weak Allee effects and fear effects into a Leslie–Gower framework, whereas our model does not include these effects but instead combines Smith growth with ratio-dependent predation.

Furthermore, investigating diffusion-driven Turing bifurcation is of great ecological value. The Turing bifurcation condition allows one to quantify the critical diffusion ratio beyond which the homogeneous steady state becomes unstable and spatially heterogeneous patterns emerge. Such transitions have been studied in various ecological and biological contexts (see, e.g., [8–11]).

Related phenomena such as Hopf bifurcation [12], Turing instability [8], and pattern formation [9–11] have been extensively studied in reaction–diffusion models. Recent investigations have also explored prey-taxis mechanisms [13] and traveling wave solutions in fractional-order predator–prey systems [14], which are complementary to the bifurcation analysis presented here.

Related studies on stability, threshold dynamics, and diffusion-induced pattern formation in biological systems can be found in [15–17].

In particular, [18] examined pattern dynamics in a harvested predator–prey model.

Motivated by [2, 19] and considering the diffusion factor, we examine the following diffusive predator–prey model with a ratio-dependent Holling type III functional response and Smith growth:

$$\begin{cases} \dfrac{\partial \omega(x,t)}{\partial t} = D_1 \Delta \omega(x,t) + \dfrac{\omega(x,t)(1-\omega(x,t))}{1+c\omega(x,t)} - \dfrac{\alpha(m+1)\omega^2(x,t)u(x,t)}{\omega^2(x,t)+mu^2(x,t)} - H\omega(x,t), \\ \dfrac{\partial u(x,t)}{\partial t} = D_2 \Delta u(x,t) + \lambda u(x,t)\left(1 - \dfrac{u(x,t)}{\omega(x,t)}\right), \end{cases} \tag{1.1}$$

with the homogeneous Neumann boundary conditions

$$\frac{\partial \omega}{\partial n} = \frac{\partial u}{\partial n} = 0, \quad x \in \partial\Omega, \tag{1.2}$$

where the spatial domain is $\Omega = (0, \pi)$. The state variables $\omega(x,t)$ and $u(x,t)$ denote the prey and predator densities, respectively. Spatial dispersal is governed by the Laplacian Δ, with D_1 and D_2 representing the prey and predator diffusion rates. The key biological parameters are predation

efficiency $\alpha \in (0, 1)$, predator growth rate $\lambda > 0$, environmental adaptation $c \geq 0$ (typically $c \ll 1$) [5], half-saturation threshold $m \in (0, 1)$ (ensuring $b_{12} < 0$), and prey harvesting rate $H \in (0, 1 - \alpha)$ [18]. The model incorporates a ratio-dependent Holling type III functional response $\frac{\alpha(m+1)\omega^2}{\omega^2+mu^2}$ [19, 20], a Leslie–Gower predator dynamics term $\lambda u(1 - u/\omega)$ [4], and a prey harvesting term $H\omega$ [18]. All parameters are positive. The proposed model is constructed under the following explicit biological assumptions:

- Prey growth (Smith growth [1, 21]): The per-capita growth rate of the prey is of the form $\frac{1-\omega}{1+c\omega}$, which decreases with prey density ω for $c > 0$ and approaches linear decay in the limit $c \to 0$. This form is appropriate for species exhibiting strong intraspecific competition or territoriality, such as certain fish stocks or insect populations under resource-limited conditions.
- Functional response (ratio-dependent Holling type III [19]): Predators exhibit a learning or search-image formation, leading to low predation efficiency at very low prey densities, accelerating at intermediate densities, and saturating at high densities. The ratio-dependent form further incorporates predator interference, making it suitable for systems where predator density directly affects foraging efficiency (e.g., invertebrate predators or planktivorous fish).
- Predator growth (Leslie–Gower [22]): The predator's carrying capacity is proportional to prey abundance, and the predator dynamics depend on per-capita prey availability rather than absolute prey density. This is a common assumption for generalist predators that switch to alternative prey when the focal prey is scarce.

Consequently, the model is applicable to predator–prey systems such as zooplankton–phytoplankton, mite–mite, or certain fish–invertebrate communities in spatially heterogeneous environments. It is not intended for systems with a type I or type II functional response, nor for those where predator growth follows a purely Lotka–Volterra scheme.

Before outlining the structure of the paper, we clarify our terminology regarding the interaction between spatial and temporal instabilities. Because we have only established a linear threshold for temporal oscillations, we avoid the term "Turing–Hopf bifurcation" and instead describe dynamical phenomena near the intersection of the Turing bifurcation curve and the linear Hopf threshold. Here, spatially inhomogeneous steady states, spatially inhomogeneous periodic solutions, and homogeneous limit cycles may coexist or compete. A complete codimension-two analysis at the intersection point, requiring center manifold reduction and normal-form computation, is beyond the scope of this paper and remains a subject for future nonlinear analysis. Our theoretical results focus on the separate derivation of Turing bifurcation conditions and the linear Hopf threshold, alongside the rigorous treatment of the Turing branch. The complex patterns near the intersection are explored numerically in Section 4.

The rest of this paper is organized as follows. In Section 2, we present the diffusive predator–prey model and derive the conditions under which Turing and Hopf bifurcations occur. Section 3 focuses on the bifurcation analysis of the steady-state problem, where we prove the local existence of non-constant steady states. Section 4 contains numerical simulations that support our theoretical results. Section 5 offers some concluding remarks.

2. Linear stability analysis and derivation of bifurcation thresholds

For the domain $(0,\pi)$ with Neumann boundary conditions, the eigenvalues of $-\Delta$ are $\mu_i = i^2$ ($i = 0,1,2,\dots$) with eigenfunctions $\cos(ix)$. Here and throughout the paper, we use μ_i (with subscript i) exclusively for the Laplacian eigenvalues, while the temporal spectral parameter in the characteristic equation is denoted by μ (without subscript), consistent with the standard notation in bifurcation theory. Set

$$\begin{cases} F(\omega,u) = \dfrac{\omega(1-\omega)}{1+c\omega} - \dfrac{\alpha(m+1)\omega^2 u}{\omega^2+mu^2} - H\omega, \\ G(\omega,u) = \lambda u\left(1-\dfrac{u}{\omega}\right). \end{cases} \tag{2.1}$$

System (1.1) possesses a strictly positive steady-state

$$E^* = (\omega^*, u^*) = \left(\frac{1-\alpha-H}{1+c(\alpha+H)}, \frac{1-\alpha-H}{1+c(\alpha+H)}\right),$$

provided $\alpha + H < 1$. Note that $1 + c(\alpha + H) > 0$ always holds for positive parameters, so E^* is well-defined and positive if and only if $\alpha + H < 1$.

Remark 2.1. ***Parameter assumptions.*** *Throughout this paper, we impose the following parameter restrictions:*

(i) $\alpha + H < 1$, *which ensures the existence of a positive equilibrium* E^* *(see above);*
(ii) $\mathscr{U}_\beta > 0$, *where* $\mathscr{U}_\beta$ *is defined in (2.7), which guarantees that the polynomial* $\mathbf{P}(H)$ *attains a positive maximum for* $H > 0$ *and hence that a Turing instability can occur (see the analysis of* $\mathbf{P}(H)$ *in this section);*
(iii) $D_{2,j} > 0$ *for the critical mode* j, *as defined in Theorem 3.1, which ensures that the bifurcation parameter* D_2 *is physically admissible;*
(iv) the spectral separation condition: For a selected critical mode $j \in \mathbb{N}^+$, *the critical diffusion coefficient* D_j *is positive, the homogeneous mode is non-singular (*$\det \mathbf{B} \neq 0$*), and the modal matrices satisfy* $\det\left[\mathbf{B} - \operatorname{diag}(D_1\mu_i, D_j\mu_i)\right] \neq 0$ *for all* $i \in \mathbb{N}_0 \setminus \{j\}$. *This guarantees that the critical mode* j *is isolated, avoiding multiple-eigenvalue interactions so that the simple-eigenvalue bifurcation theorem applies (see Theorem 3.1).*

These conditions are assumed throughout the paper without further mention, and all parameter choices in the numerical simulations in Section 4 satisfy them.

The Jacobian linearization about this equilibrium yields

$$\begin{pmatrix} \frac{\partial \omega}{\partial t} \\ \frac{\partial u}{\partial t} \end{pmatrix} = \mathbf{D}\Delta \begin{pmatrix} \omega \\ u \end{pmatrix} + \mathbf{B}\begin{pmatrix} \omega \\ u \end{pmatrix}, \tag{2.2}$$

with

$$\mathbf{D}\Delta = \begin{pmatrix} D_1\Delta & 0 \\ 0 & D_2\Delta \end{pmatrix}, \quad \mathbf{B} = \begin{pmatrix} b_{11} & b_{12} \\ b_{21} & b_{22} \end{pmatrix},$$

where

$$
\begin{aligned}
b_{11} &= \frac{c(\alpha+H)^2+2(\alpha+H)-1}{1+c} - \frac{2\alpha m}{1+m} - H,\\
b_{12} &= -\frac{\alpha(1-m)}{1+m} < 0,\\
b_{21} &= \lambda > 0,\\
b_{22} &= -\lambda < 0.
\end{aligned}
$$

The characteristic polynomial of the linearized system takes the form

$$\det(\mu\mathbf{I} - \mathbf{B_h}) = 0,$$

where $\mathbf{B_h} = \mathbf{B} - diag\{D_1h^2,\ D_2h^2\},\ h > 0$. That is,

$$
\begin{aligned}
|\mu\mathbf{I} - \mathbf{B_h}| &= \begin{vmatrix} \mu - b_{11} + D_1h^2 & -b_{12} \\ -b_{21} & \mu - b_{22} + D_2h^2 \end{vmatrix}\\
&= \mu^2 + \Big[(D_1+D_2)h^2 - (b_{11}+b_{22})\Big]\mu\\
&\quad + D_1D_2h^4 - (b_{11}D_2 + D_1b_{22})\,h^2 + (b_{11}b_{22} - b_{12}b_{21})\,.
\end{aligned}
$$

The equation reduces to the following quadratic:

$$\Delta_h(\mu) = \mu^2 + \mathscr{T}_h\mu + \mathscr{R}_h = 0, \tag{2.3}$$

where

$$\mathscr{T}_h = (D_1+D_2)h^2 - (b_{11}+b_{22}), \tag{2.4}$$

$$\mathscr{R}_h = D_1D_2h^4 - (b_{11}D_2 + D_1b_{22})\,h^2 + (b_{11}b_{22} - b_{12}b_{21})\,. \tag{2.5}$$

Turing instability arises if $\mathscr{R}_h < 0$ for some $h > 0$. The Turing bifurcation curve in the $D_2 - \lambda$ plane is defined by $\mathscr{R}_h = 0$.

In the absence of diffusion ($h = 0$), asymptotic stability of the equilibrium E^* requires both the trace condition ($\mathscr{T}_0 > 0$) and the determinant condition ($\mathscr{R}_0 > 0$). Assuming these homogeneous stability conditions are satisfied, nevertheless, under conditions where

$$\lambda > \frac{c(\alpha+H)^2+2(\alpha+H)-1}{1+c} - \frac{2\alpha m}{1+m} - H,$$

the Turing instability arises when $\mathscr{R}_h < 0$ for any $h > 0$, a phenomenon known as diffusion-induced instability. In the $D_2 - \lambda$ parameter space, the Turing bifurcation boundary is characterized by $\mathscr{R}_h = 0$. As shown in Eq (2.5), this boundary consists of straight lines whose slopes are determined by $\rho(h)$.

$$\rho(h) \equiv -\frac{\mathscr{Z}_h}{\mathscr{Y}_h} = -\frac{D_1h^4 - \mathscr{U}_\beta h^2}{D_1h^2 + \mathscr{V}_\beta}, \tag{2.6}$$

where

$$\begin{aligned}
\mathscr{Z}_h &= D_1 h^4 - \left(\frac{c(\alpha+H)^2 + 2(\alpha+H) - 1}{1+c} - \frac{2\alpha m}{1+m} - H \right) h^2 = D_1 h^4 - \mathscr{U}_\beta h^2, \\
\mathscr{Y}_h &= D_1 h^2 - \frac{c(\alpha+H)^2 + (1-c)(\alpha+H) - 1}{1+c} = D_1 h^2 + \mathscr{V}_\beta, \\
\mathscr{U}_\beta &= \frac{c(\alpha+H)^2 + 2(\alpha+H) - 1}{1+c} - \frac{2\alpha m}{1+m} - H, \\
\mathscr{V}_\beta &= \frac{\alpha(1-m)}{1+m} - \mathscr{U}_\beta = \frac{(1+c\alpha+cH)(1-\alpha-H)}{c+1} > 0.
\end{aligned} \tag{2.7}$$

Examining these linear boundaries allows us to explore the stability characteristics of the system within the $D_2 - \lambda$ parameter space and determine the specific requirements for the emergence of Turing instability. Setting $\eta = h^2$, where η denotes a continuous spectral variable and $h \in \mathbb{N}_0$ is the discrete Neumann mode index, we define the rational function

$$\mathbf{P}(\eta) = -\frac{D_1\eta^2 - \mathscr{U}_\beta \eta}{D_1\eta + \mathscr{V}_\beta}.$$

Consequently, $\mathbf{P}(\eta)$ has zeros at $\eta = 0$ and $\eta = \frac{\mathscr{U}_\beta}{D_1}$ and a singularity at $\eta = -\frac{\mathscr{V}_\beta}{D_1}$. The derivative of $\mathbf{P}(\eta)$ is

$$\mathbf{P}'(\eta) = -\frac{D_1^2\eta^2 + 2D_1\mathscr{V}_\beta\eta - \mathscr{U}_\beta\mathscr{V}_\beta}{(D_1\eta + \mathscr{V}_\beta)^2}.$$

The critical points of $\mathbf{P}(\eta)$ are obtained by solving $\mathbf{P}'(\eta) = 0$. This yields two distinct roots, which we consistently denote as η_1 (the negative root) and η_2 (the positive root whenever $\mathscr{U}_\beta > 0$):

$$\begin{aligned}
\eta_1 &= \frac{-\mathscr{V}_\beta - \sqrt{\mathscr{V}_\beta(\mathscr{V}_\beta + \mathscr{U}_\beta)}}{D_1} < 0, \\
\eta_2 &= \frac{-\mathscr{V}_\beta + \sqrt{\mathscr{V}_\beta(\mathscr{V}_\beta + \mathscr{U}_\beta)}}{D_1} > 0, \quad \text{if } \mathscr{U}_\beta > 0.
\end{aligned}$$

To analyze the location of these roots relative to the singularity $-\frac{\mathscr{V}_\beta}{D_1}$ and the zero $\frac{\mathscr{U}_\beta}{D_1}$, we observe that

$$\begin{aligned}
-\frac{\mathscr{V}_\beta}{D_1} - \eta_1 &= \frac{\sqrt{\mathscr{V}_\beta(\mathscr{V}_\beta + \mathscr{U}_\beta)}}{D_1} > 0, \\
-\frac{\mathscr{V}_\beta}{D_1} - \eta_2 &= -\frac{\sqrt{\mathscr{V}_\beta(\mathscr{V}_\beta + \mathscr{U}_\beta)}}{D_1} < 0, \\
-\frac{\mathscr{V}_\beta}{D_1} - \frac{\mathscr{U}_\beta}{D_1} &= -\frac{\alpha(1-m)}{D_1(1+m)} < 0.
\end{aligned}$$

When $\mathscr{U}_\beta > 0$, the roots are strictly ordered as

$$\eta_1 < -\frac{\mathscr{V}_\beta}{D_1} < 0 < \eta_2 < \frac{\mathscr{U}_\beta}{D_1}. \tag{2.8}$$

When $\mathscr{U}_\beta < 0$, the order becomes

$$\eta_1 < -\frac{\mathscr{V}_\beta}{D_1} < \frac{\mathscr{U}_\beta}{D_1} < \eta_2 < 0. \tag{2.9}$$

Furthermore, the limits around the singularity are

$$\lim_{\eta\to-\frac{\mathscr{V}_\beta}{D_1}^-}\mathbf{P}'(\eta)=+\infty,\qquad \lim_{\eta\to-\frac{\mathscr{V}_\beta}{D_1}^+}\mathbf{P}'(\eta)=+\infty, \tag{2.10}$$

$$\lim_{\eta\to-\frac{\mathscr{V}_\beta}{D_1}^-}\mathbf{P}(\eta)=+\infty,\qquad \lim_{\eta\to-\frac{\mathscr{V}_\beta}{D_1}^+}\mathbf{P}(\eta)=-\infty. \tag{2.11}$$

An analysis of Eqs (2.8) and (2.11) reveals that for strictly positive values of η, the inequality $\mathbf{P}(\eta) > 0$ is valid exclusively when $\mathscr{V}_\beta$ is positive. Therefore, under the condition $\mathscr{V}_\beta > 0$, the rational function satisfies $\mathbf{P}(\eta) > 0$ within the interval $(0, \frac{\mathscr{V}_\beta}{D_1})$, attaining its maximum value $\rho_{\max}(h) = \mathbf{P}(\eta_2)$ evaluated at the continuous variable $h = \sqrt{\eta_2}$.

Reference [2] analyzes Hopf bifurcation and delay-induced periodic dynamics in a diffusive predator–prey model with Smith growth and herd behavior. Building upon such foundational bifurcation studies, the present work further investigates the interaction between the Turing instability and the linear Hopf threshold in a system with a ratio-dependent functional response.

Remark 2.2. *For the homogeneous mode $h = 0$, the characteristic polynomial reduces to $\mu^2 - (b_{11} + b_{22})\mu + (b_{11}b_{22} - b_{12}b_{21}) = 0$. Since $b_{22} = -\lambda < 0$ and $b_{21} = \lambda > 0$, a linear Hopf threshold occurs at $\lambda = U_\beta$ (where $U_\beta > 0$), with imaginary frequency $\omega_H = \sqrt{U_\beta V_\beta}$. This condition is necessary for the existence of a Hopf bifurcation, but it is not sufficient unless transversality, simplicity of the conjugate pair, and exclusion of all nonzero spatial modes at the same parameter value are verified. In this paper, we do not pursue the full Hopf theorem (including direction and stability of the periodic orbit), which would require the computation of the first Lyapunov coefficient. Our numerical examples in Section 4 illustrate the emergence of periodic solutions near the Hopf curve, but their analytical validation is left for future work.*

3. Steady-state bifurcation analysis

The conditions for Turing bifurcation and the linear Hopf threshold having been obtained in Section 2, we now turn to the Turing branch. Since this is a steady-state bifurcation from the constant equilibrium, the present section is concerned with the local existence of the non-constant steady states that bifurcate from it. The interaction between the Turing branch and the Hopf-type oscillatory branch near their intersection will be investigated numerically in Section 4.

The local structure of steady states arising from a simple eigenvalue is studied in this section. The case of a simple eigenvalue is handled via the Crandall–Rabinowitz theorem [23]. The analysis of multiple eigenvalue interactions requires a higher-dimensional Lyapunov–Schmidt reduction and is beyond the scope of the present work. Therefore, we restrict our analytical bifurcation result to the simple eigenvalue case.

Hence, we focus on the steady-state problem associated with model (1.1):

$$\begin{cases} -D_1\omega_{xx} = \frac{\omega(1-\omega)}{1+c\omega} - \frac{\alpha(m+1)\omega^2 u}{\omega^2+mu^2} - H\omega, & x\in(0,\pi),\\ -D_2u_{xx} = \lambda u\left(1-\frac{u}{\omega}\right), & x\in(0,\pi),\\ \omega_x = u_x = 0, & x\in\partial\Omega. \end{cases} \tag{3.1}$$

We first shift the equilibrium (ω^*, u^*) to the origin by introducing the transformation $(\overline{\omega}, \overline{u}) = (\omega - \omega^*, u - u^*)$. For notational simplicity, we continue to denote $\overline{\omega}$ and $\overline{u}$ by ω and u respectively, which yields

$$\begin{cases} -D_1\omega_{xx} = f(\omega + \omega^*, u + u^*), & x \in (0, \pi), \\ -D_2 u_{xx} = g(\omega + \omega^*, u + u^*), & x \in (0, \pi), \\ \omega_x = u_x = 0, & x \in \partial\Omega, \end{cases} \tag{3.2}$$

where

$$f(\omega + \omega^*, u + u^*) = \frac{(\omega + \omega^*)(1 - \omega - \omega^*)}{1 + c(\omega + \omega^*)} - \frac{\alpha(m+1)(\omega + \omega^*)^2(u + u^*)}{(\omega + \omega^*)^2 + m(u + u^*)^2} - H(\omega + \omega^*),$$

$$g(\omega + \omega^*, u + u^*) = \lambda(u + u^*)\left(1 - \frac{u + u^*}{\omega + \omega^*}\right).$$

3.1. Local bifurcation

By treating D_2 as the bifurcation parameter, we prove the existence of positive solutions that bifurcate from the point $(D_2, 0, 0)$. To rigorously apply the Crandall–Rabinowitz theorem and accommodate the subsequent inner-product and adjoint-operator arguments, we restrict our analysis to a standard Hilbert-space framework. Let

$$\mathbb{X} = \left\{(\omega, u) \in H^2(0, \pi) \times H^2(0, \pi) : \omega_x(0) = \omega_x(\pi) = 0, \quad u_x(0) = u_x(\pi) = 0\right\},$$

and

$$\mathbb{Y} = L^2(0, \pi) \times L^2(0, \pi).$$

Equipped with their standard Sobolev and Lebesgue norms, both $\mathbb{X}$ and $\mathbb{Y}$ are Hilbert spaces.

Because the reaction terms in $\mathcal{F}$ contain denominators $1 + c(\omega + \omega^*)$ and $(\omega + \omega^*)^2 + m(u + u^*)^2$, we must restrict the domain of the operator to avoid singularities. We define an open neighborhood of the origin in $\mathbb{X}$:

$$\mathcal{O} = \left\{(\omega, u) \in \mathbb{X} : \min_{x \in [0,\pi]} (\omega(x) + \omega^*) > 0, \ \min_{x \in [0,\pi]} (u(x) + u^*) > 0\right\}.$$

By the Sobolev embedding theorem, $H^2(0, \pi) \hookrightarrow C([0, \pi])$, ensuring that functions in $\mathcal{O}$ are continuous and their minimums are well-defined. Within this neighborhood $\mathcal{O}$, all denominators remain strictly positive. We then define the map

$$\mathcal{F} : (0, \infty) \times \mathcal{O} \to \mathbb{Y}$$

by

$$\mathcal{F}(D_2, \omega, u) = \begin{pmatrix} D_1\omega_{xx} + f(\omega + \omega^*, u + u^*) \\ D_2 u_{xx} + g(\omega + \omega^*, u + u^*) \end{pmatrix}.$$

Because rational functions with non-vanishing denominators are smooth, the operator $\mathcal{F}$ is continuously Fréchet differentiable with respect to (D_2, ω, u) in the neighborhood $\mathcal{O}$ of $(D_j, 0, 0)$.

The Fréchet derivative of $\mathcal{F}$ with respect to (ω, u) evaluated at $(D_2, 0, 0)$ is

$$\mathcal{L}_1(D_2) = \mathcal{F}_{(\omega,u)}(D_2, 0, 0) : \mathbb{X} \to \mathbb{Y},$$

where

$$\mathcal{L}_1(D_2) = \begin{pmatrix} D_1\dfrac{\partial^2}{\partial x^2} + b_{11} & b_{12} \\ b_{21} & D_2\dfrac{\partial^2}{\partial x^2} + b_{22} \end{pmatrix}.$$

According to the standard elliptic operator theory for boundary value problems, since $\mathcal{L}_1(D_2)$ is a strongly elliptic operator with regular Neumann boundary conditions on a bounded domain, $\mathcal{L}_1(D_2)$ is a Fredholm operator of index zero.

Throughout this section, we use the normalized Neumann eigenbasis

$$\varphi_0 = \frac{1}{\sqrt{\pi}}, \qquad \varphi_k = \sqrt{\frac{2}{\pi}}\cos(kx) \quad (k \geq 1),$$

which satisfies $\int_0^\pi \varphi_k^2\, dx = 1$ for all $k \geq 0$.

Theorem 3.1. *The critical diffusion coefficient is defined by*

$$D_j = \frac{b_{12}b_{21} - \lambda(D_1\mu_j - b_{11})}{\mu_j(D_1\mu_j - b_{11})}, \tag{3.3}$$

where $\mu_j = j^2$, $j \in \mathbb{N}^+$.

Assume that for a selected positive integer j, the critical diffusion coefficient is positive ($D_j > 0$), the homogeneous mode is non-singular ($\det \mathbf{B} = b_{11}b_{22} - b_{12}b_{21} \neq 0$), and the spectral separation condition holds:

$$\det\Big[\mathbf{B} - \operatorname{diag}\big(D_1\mu_i, D_j\mu_i\big)\Big] \neq 0 \qquad \text{for all } i \in \mathbb{N}_0 \setminus \{j\}. \tag{3.4}$$

Then the kernel of $\mathcal{L}_1(D_j)$ is one-dimensional, and $(D_j, 0, 0)$ is a bifurcation point of $\mathcal{F}(D_2, \omega, u) = 0$.

Moreover, for sufficiently small $|s|$, there exists a one-parameter family of nontrivial solutions $\Gamma_j(s) = (D_2(s), \omega(s), u(s))$ such that

$$D_2(0) = D_j, \qquad (\omega(0), u(0)) = (0, 0),$$

and

$$\omega(s) = s\varphi_j + o(s), \qquad u(s) = sa_j\varphi_j + o(s),$$

where $a_j = \frac{D_1\mu_j - b_{11}}{b_{12}}$. The kernel vector associated with the zero eigenvalue is $\Phi_j = \binom{1}{a_j}\varphi_j$.

Furthermore, because the coexisting equilibrium $E^* = (\omega^*, u^*)$ is strictly positive, these local branches correspond to strictly positive prey and predator densities $\omega(s) + \omega^* > 0$ and $u(s) + u^* > 0$ in the original variables for sufficiently small $|s|$.

Proof. According to the Crandall–Rabinowitz bifurcation theorem [23], the point $(D_j, 0, 0)$ is a bifurcation point if the following conditions are met:

(i) The partial derivatives $\mathcal{F}_{D_2}$, $\mathcal{F}_{(\omega,u)}$, and $\mathcal{F}_{D_2,(\omega,u)}$ exist and are continuous.

(ii) For $D_2 = D_j$, the kernel of $\mathcal{L}_1(D_j)$ is

$$\ker \mathcal{L}_1(D_j) = \operatorname{span}\{\Phi_j\},$$

where

$$\Phi_j = \begin{pmatrix} 1 \\ a_j \end{pmatrix}\varphi_j.$$

Therefore,

$$\dim\ker \mathcal{L}_1(D_j) = 1.$$

Because $\mathcal{L}_1(D_j)$ is Fredholm of index zero,

$$\operatorname{codim}\operatorname{Im}\mathcal{L}_1(D_j) = \dim\ker \mathcal{L}_1(D_j) = 1.$$

(iii) Let $\ker \mathcal{F}_{(\omega,u)}(D_j, 0, 0) = \operatorname{span}\{\Phi_j\}$; then

$$\mathcal{F}_{D_2(\omega,u)}(D_j, 0, 0)\Phi_j \notin \operatorname{Im}\left(\mathcal{F}_{(\omega,u)}(D_j, 0, 0)\right).$$

We now verify conditions (i)–(iii). For $D_2 = D_j$, the operator $\mathcal{L}_1(D_2)$ is given by

$$\mathcal{L}_1\left(D_j\right) = \mathcal{F}_{(\omega,u)}\left(D_2, 0, 0\right) = \begin{pmatrix} D_1\frac{\partial^2}{\partial x^2} + b_{11} & b_{12} \\ b_{21} & D_j\frac{\partial^2}{\partial x^2} + b_{22} \end{pmatrix}.$$

The continuity of the linear operators $\mathcal{F}_{(\omega,u)}$, $\mathcal{F}_{D_2(\omega,u)}$, and $\mathcal{F}_{D_2}$ is evident, thereby satisfying condition (i).

Now, let $\Phi = (\widetilde{\varphi}, \widetilde{\psi})^\top \in \ker \mathcal{L}_1(D_j)$, and express $\widetilde{\varphi} = \sum_i \widetilde{b}_i\varphi_i$ and $\widetilde{\psi} = \sum_i \widetilde{a}_i\varphi_i$. Then

$$\sum_{i=0}^{\infty} \widetilde{\mathcal{B}}_i \begin{pmatrix} \widetilde{b}_i \\ \widetilde{a}_i \end{pmatrix} \varphi_i = 0, \quad \text{where} \quad \widetilde{\mathcal{B}}_i = \mathbf{B} - \operatorname{diag}(D_1\mu_i, D_j\mu_i) = \begin{pmatrix} b_{11} - D_1\mu_i & b_{12} \\ b_{21} & b_{22} - D_j\mu_i \end{pmatrix}. \tag{3.5}$$

By the definition of D_j, it directly follows that $\det\widetilde{\mathcal{B}}_j = 0$. For the homogeneous mode ($i = 0$), we have $\widetilde{\mathcal{B}}_0 = \mathbf{B}$. The hypothesis explicitly guarantees $\det\widetilde{\mathcal{B}}_0 = \det\mathbf{B} = b_{11}b_{22} - b_{12}b_{21} \neq 0$. For any other spatial mode $i \in \mathbb{N}^+ \setminus \{j\}$, the spectral separation hypothesis directly assumes $\det\widetilde{\mathcal{B}}_i \neq 0$. This rigorously avoids the undefined quotient (D_i) for any mode where $\mu_i(D_1\mu_i - b_{11}) = 0$. Consequently, the condition $\det\widetilde{\mathcal{B}}_i = 0$ holds if and only if $i = j$, which naturally extends to the adjoint operator as $\det\widetilde{\mathcal{B}}_i^\top = \det\widetilde{\mathcal{B}}_i$. This gives:

$$\ker \mathcal{L}_1 = \operatorname{span}\left\{\Phi_j\right\}, \ \Phi_j = \begin{pmatrix} 1 \\ a_j \end{pmatrix}\varphi_j \ , \ \text{where} \ \ a_j = \frac{D_1\mu_j - b_{11}}{b_{12}}.$$

A direct calculation gives

$$\mathcal{L}_1(D_j)\Phi_j = \begin{pmatrix} D_1\varphi_j'' + b_{11}\varphi_j + b_{12}a_j\varphi_j \\ b_{21}\varphi_j + (D_j\varphi_j'' + b_{22}a_j\varphi_j) \end{pmatrix}.$$

Since

$$\varphi_j'' = -\mu_j\varphi_j,$$

the first component becomes

$$(-D_1\mu_j + b_{11} + b_{12}a_j)\varphi_j = 0.$$

Moreover,

$$(-D_j\mu_j + b_{22})a_j + b_{21} = 0,$$

which follows from the definition of D_j. Therefore,

$$\mathcal{L}_1(D_j)\Phi_j = 0.$$

Now we examine the adjoint operator

$$\mathcal{L}_1^* = \begin{pmatrix} D_1\frac{\partial^2}{\partial x^2} + b_{11} & b_{21} \\ b_{12} & D_j\frac{\partial^2}{\partial x^2} + b_{22} \end{pmatrix}.$$

Following a similar argument as above, we obtain

$$\ker \mathcal{L}_1^* = \operatorname{span}\left\{\Phi_j^*\right\}.$$

The eigenvector of the adjoint operator corresponding to the zero eigenvalue is given by

$$\Phi_j^* = \begin{pmatrix} 1 \\ a_j^* \end{pmatrix} \varphi_j,$$

where

$$a_j^* = \frac{D_1\mu_j - b_{11}}{b_{21}}.$$

By the Fredholm alternative,

$$\operatorname{Im} \mathcal{L}_1(D_j) = \ker \mathcal{L}_1^*(D_j)^{\perp}.$$

Moreover,

$$\dim \ker \mathcal{L}_1^*(D_j) = 1.$$

Hence,

$$\operatorname{codim} \operatorname{Im} \mathcal{L}_1(D_j) = 1.$$

Condition (ii) is therefore satisfied.

Finally, we evaluate the mixed derivative with respect to the diffusion parameter D_2 and the state variables (ω, u) at the bifurcation point:

$$\mathcal{F}_{D_2,(\omega,u)}(D_j, 0, 0)\Phi_j = \begin{pmatrix} 0 & 0 \\ 0 & \frac{\partial^2}{\partial x^2} \end{pmatrix} \Phi_j = \begin{pmatrix} 0 \\ -\mu_j a_j \varphi_j \end{pmatrix}.$$

Taking the inner product in the Hilbert space $\mathbb{Y} = L^2(0,\pi) \times L^2(0,\pi)$, we have

$$\langle \mathcal{F}_{D_2,(\omega,u)}(D_j, 0, 0)\Phi_j, \Phi_j^* \rangle_{\mathbb{Y}} = \int_0^{\pi} (-\mu_j a_j \varphi_j)(a_j^* \varphi_j)\, dx = -\mu_j a_j a_j^* > 0.$$

Since $\langle \mathcal{F}_{D_2,(\omega,u)}(D_j, 0, 0)\Phi_j, \Phi_j^* \rangle_{\mathbb{Y}} \neq 0$, the transversality condition is verified:

$$\mathcal{F}_{D_2,(\omega,u)}(D_j, 0, 0)\Phi_j \notin \operatorname{Im} \mathcal{L}_1(D_j).$$

Therefore, all conditions of the Crandall–Rabinowitz theorem are satisfied. This completes the proof. □

Remark 3.1. *The present analysis focuses on steady-state bifurcation caused by a simple critical eigenvalue. The interaction between multiple critical modes may generate more complicated bifurcation structures, but a rigorous analysis requires a higher-dimensional Lyapunov–Schmidt reduction, which is beyond the scope of this paper.*

4. Numerical simulations

Numerical simulations are carried out using a finite difference scheme on a uniform grid with spatial step $\Delta x = \pi/N$. Spatial derivatives are discretized using second-order centered differences:

$$\left.\frac{\partial^2\omega}{\partial x^2}\right|_{x_i} \approx \frac{\omega_{i+1} - 2\omega_i + \omega_{i-1}}{\Delta x^2}.$$

The homogeneous Neumann boundary conditions are implemented via the standard ghost-point method, setting values at the virtual points $x_{-\Delta x}$ and $x_{\pi+\Delta x}$ equal to those at $x_{\Delta x}$ and $x_{\pi-\Delta x}$, respectively. Time integration is performed using the explicit fourth-order Runge–Kutta method (RK4) with fixed time step $\Delta t = 0.001$. The initial data are taken as small perturbations of the equilibrium E^*. For general pattern formation simulations, we use

$$\omega(x, 0) = \omega^* + \varepsilon\xi_\omega(x), \qquad u(x, 0) = u^* + \varepsilon\xi_u(x),$$

where $\varepsilon = 10^{-3}$ and ξ_ω, ξ_u are independent realizations of uniform random noise on $[-1, 1]$. We explicitly utilize the exact random seed for the pseudo-random number generator to guarantee strict reproducibility. However, for the rigorous convergence tests (see Remark 4.1), we prescribe a fixed smooth perturbation to ensure all grids represent the exact same continuous initial function.

To handle the singular term u/ω when ω becomes very small, we impose a small numerical cutoff: Whenever $\omega < 10^{-12}$, we set $\omega = 10^{-12}$ in the computation of this term. We systematically monitored the minimum prey density throughout the integration for each parameter case. For all simulations reported below, the exact global minimum prey density strictly satisfies $\min_{x,t} \omega(x, t) > 10^{-6}$ (typically remaining on the order of 10^{-5} at its lowest point). Consequently, exactly zero cutoff activations occurred at any time during the simulations. While the numerical preservation of these positive values provides strong computational evidence that the system maintains positivity without artificial intervention, we acknowledge that it does not constitute a rigorous mathematical proof of positivity. For most parameter sets, simulations are run until a final time $T = 1000$, which is generally sufficient to ensure that transient behaviors have decayed. The solution is sampled every $\Delta t_{\text{out}} = 0.1$ time units for analysis. However, in regimes near the bifurcation boundary where exceptionally slow decay modes exist, simulations are explicitly extended to much longer time scales (e.g., $T = 10^5$) to guarantee the accurate resolution of the eventual asymptotic behavior.

Remark 4.1. ***Spatial and temporal convergence.*** *Spatial convergence is verified by systematic grid refinement evaluated at the stable parameter point $P_1(D_2 = 0.06, \lambda = 0.19)$. To avoid temporal phase differences that may pollute the true discretization error for long-term or periodic solutions, we conduct a short-time test comparing the solutions at final time $T = 1.0$. The initial condition is prescribed as a fixed smooth perturbation: $\omega(x, 0) = \omega^* + 10^{-3}\cos(x)$ and $u(x, 0) = u^* + 10^{-3}\cos(x)$, ensuring all grids sample the identical continuous function.*

We compute the relative L^2-error for both the prey (ω) and predator (u) variables with respect to a reference solution on a finer grid with $N_{\text{ref}} = 800$ intervals. Since the coarse grids ($N = 100, 200, 400$) are nested within the reference grid, the transfer procedure is a direct injection (subsampling) of the fine-grid values at the coincident node locations. The discrete L^2-norm is approximated using the composite trapezoidal quadrature rule:

$$E_{N,\omega} = \frac{\|\omega_N - \omega_{800}\|_{L^2}}{\|\omega_{800}\|_{L^2}}, \quad \|\omega\|_{L^2} = \left(\frac{\Delta x}{2}\sum_{i=0}^{N-1}(\omega_i^2 + \omega_{i+1}^2)\right)^{1/2},$$

and similarly for $E_{N,u}$.

To establish rigorous numerical stability for the fully coupled semi-discrete system, we explicitly evaluate the complex spectrum of the full reaction–diffusion Jacobian $\mathbf{J}$*. By applying the Gershgorin circle theorem, the eigenvalues* z *of* $\mathbf{J}$ *are enclosed in complex disks centered at* J_{ii} *with radii* $\sum_{j\neq i}|J_{ij}|$*.*

For the spatial convergence test evaluated at the stable point P_1*, the initial perturbation is tightly confined near the equilibrium. Over the dynamically admissible tight region for this short-time test* $(\omega, u \in [0.08, 0.09])$*, we analytically recalculate the maximum infinity norm of the complete reaction Jacobian matrix, yielding a precise bound* $L \approx 1.2$*. On the finest grid* ($N = 800$, $\Delta x \approx 0.0039$)*, the scaled discrete Laplacian contributes extreme negative real eigenvalues down to* $-4\max(D_1, D_2)/(\Delta x)^2 \approx -15584$*. The full complex spectral enclosure is thus tightly bounded within* $Re(z) \in [-15585, 1.2]$ *with the imaginary spectral radius bounded by* L*.*

To conclusively isolate spatial error, we repeated the convergence test using exactly one common stable time step $\Delta t = 5 \times 10^{-5}$ *for all grids. The scaled spectrum* $\Delta t z$ *falls within* $Re(\Delta t z) \in [-0.78, 0.00006]$*, well inside the complex RK4 stability domain, ensuring* $|R_{\mathrm{RK4}}(\Delta t z)| \leq 1$ *for all damped modes. To confirm that the reported second-order convergence reflects pure spatial error rather than residual temporal error, a temporal refinement test at* $N = 200$ *(reducing* Δt *from* 5×10^{-5} *to* 2.5×10^{-5}*) yielded a relative difference below* 10^{-8}*. The isolated pure spatial errors at* $T = 1.0$ *are*

$$E_{100,\omega} \approx 1.2 \times 10^{-3}, \quad E_{200,\omega} \approx 3.0 \times 10^{-4}, \quad E_{400,\omega} \approx 7.5 \times 10^{-5},$$

$$E_{100,u} \approx 1.1 \times 10^{-3}, \quad E_{200,u} \approx 2.8 \times 10^{-4}, \quad E_{400,u} \approx 7.0 \times 10^{-5},$$

indicating a conclusive second-order spatial convergence rate (the error ratio is approximately 4).

For the long-time pattern formation simulations on the working grid $N = 200$*, the state variables cover a wider region, dropping to reported minimums near* 10^{-5}*. Because the predator density naturally drops concurrently with the prey density, the potentially singular ratio* u/ω *remains strictly bounded, keeping the reaction Jacobian norm bounded* ($L \sim O(10^1)$)*. With* $N = 200$ ($\Delta x \approx 0.0157$)*, the maximum diffusive eigenvalue magnitude reduces to* ≈ 974*. At the selected time step* $\Delta t = 0.001$*, the scaled negative spectrum extends to roughly* -0.97*, comfortably satisfying the absolute stability condition for all damped spatial modes. Finally, we must explicitly distinguish damped modes from physically unstable modes: At parameter points* P_3 *and* P_4*, the system possesses physically unstable modes with* $Re(z) > 0$*. For these specific eigenvalues, the numerical amplification correctly yields* $|R_{\mathrm{RK4}}(\Delta t z)| > 1$*, accurately reflecting the physical growth that drives pattern formation, while all high-frequency dispersive modes remain strictly damped* ($|R_{\mathrm{RK4}}| \leq 1$)*. Spatial and temporal errors have thus been safely and consistently assessed.*

For the spatial discretization, the one-dimensional domain $[0, \pi]$ is divided into N uniform mesh intervals. The diffusion terms are approximated by the standard second-order finite difference scheme, and the homogeneous Neumann boundary conditions are implemented using the corresponding discrete boundary conditions.

Given $\alpha = 0.8$, $m = 0.5$, $c = 0.2$, $H = 0.1$, and $D_1 = 0.016$, after some straightforward calculations, we determine that the positive equilibrium is $E^* = (\omega^*, u^*) = (0.0847, 0.0847)$ and $\sqrt{\eta_2} \approx 1.994$. Since the continuous maximum of $\rho(h)$ is attained at $\sqrt{\eta_2} \approx 1.994$, the maximum among integer modes occurs at $h = 2$ (the nearest integer). We therefore set $h = 2$ as the critical mode in the subsequent analysis. Evaluating the function ρ at this point gives us $\rho(1) = 1.3333$, $\rho(2) = 2.5724$, and

$\rho(3) = 0.9063$. From these results, the maximum value of $\rho(h)$ occurs at $h = 2$, i.e., $\rho_{\max}(h) = \rho(2)$ for $h \in \mathbb{Z}^*$. This finding is illustrated in Figure 1. In Figure 1(II), the points P_1, P_2, P_3, and P_4 are marked explicitly.

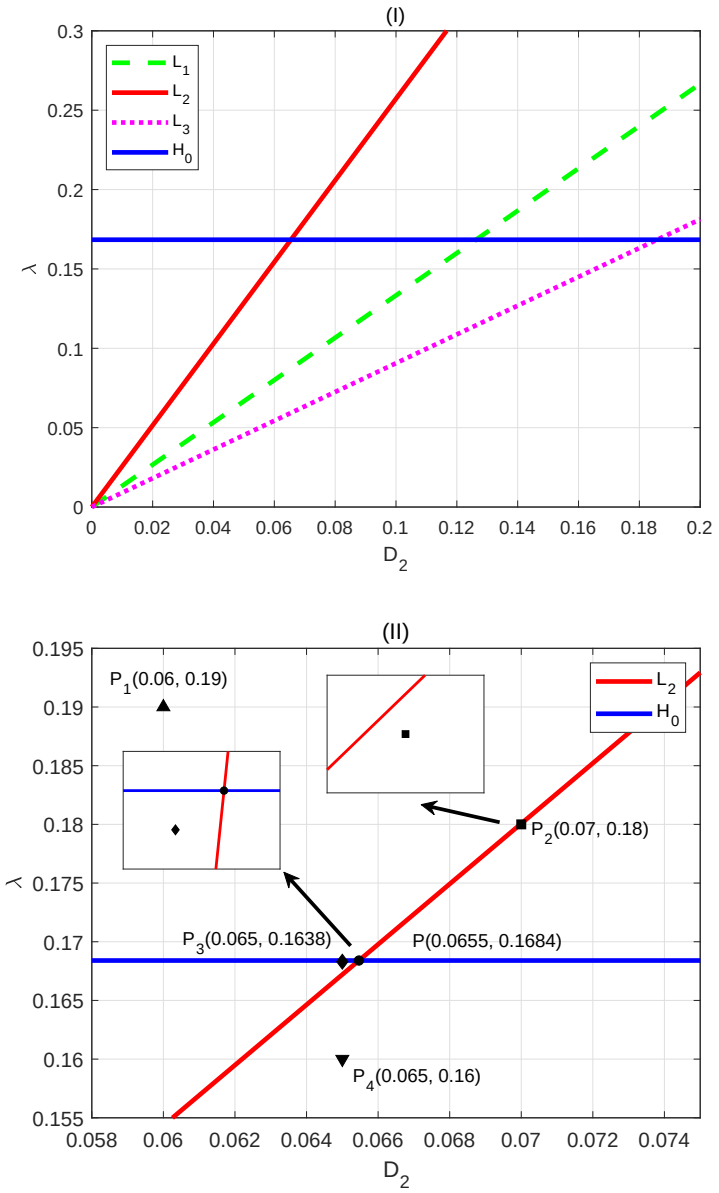

Figure 1. Two-dimensional stability region and bifurcation diagram of system (1.1) with parameters $\alpha = 0.8$, $m = 0.5$, $c = 0.2$, $H = 0.1$, and $D_1 = 0.016$. The Turing boundaries L_1–L_3 are shown as green dashed, red solid, and pink dashed curves, respectively, while the linear Hopf threshold H_0 is shown as a blue solid curve. Numerical simulations indicate that the slope of the L_h lines attains its maximum at $h = 2$. The inset in (II) shows details near the intersection point $P(0.0655, 0.1684)$ between H_0 and L_2, with marked points $P_1(0.06, 0.19)$, $P_2(0.07, 0.18)$, $P_3(0.065, 0.1638)$, and $P_4(0.065, 0.16)$.

Choosing the same parameters, we evaluate the linear stability of E^* using the characteristic equations (2.3)–(2.5). At $P_1(0.06, 0.19)$, all modes satisfy $\mathcal{R}_h > 0$ and $\mathcal{T}_h > 0$, confirming that the equilibrium is asymptotically stable (see Figure 2(I,II)). At $P_2(0.07, 0.18)$, direct evaluation gives $\mathcal{R}_2 \approx 0$ (a very small positive value) and $\mathcal{T}_2 > 0$, so the homogeneous steady state is linearly stable. A direct calculation from the reported linear coefficients at P_2 yields an extremely slow decay rate for the critical spatial mode, with an associated decay time of approximately 5.3×10^4. Consequently, at $T = 1000$, the linear amplitude retains about 98% of its initial value. Numerical integration from random initial perturbations produces a long-lived spatial pattern with a $\cos 2x$-like profile that persists strongly over the displayed initial time interval $T = 1000$ (see Figure 2(III),(IV)). To rigorously verify the eventual disappearance of this transient, we have extended the simulation for P_2 to $T = 10^5$, a time scale compatible with this slow mode. The extended computation confirms eventual decay to the uniform steady state, illustrating a slowly damped transient rather than a stable nonconstant steady state.

At $P_3(0.065, 0.1638)$, both the temporal mode ($h = 0$) and the critical spatial mode ($h = 2$) are unstable ($\mathcal{T}_0 < 0$ and $\mathcal{R}_2 < 0$), leading to a numerically robust spatially inhomogeneous periodic solution with a dominant $\cos 2x$ component (Figure 2(V),(VI)). To quantitatively support this modal analysis, we performed a spatial decomposition of the computed solution at $T = 1000$. The amplitude of the homogeneous mode $h = 0$ is approximately 0.084, while the critical spatial mode $h = 2$ has a measured amplitude of approximately 0.015, yielding a spatial variance of 1.1×10^{-4} as a measure of nonuniformity. Furthermore, the measured temporal period of the oscillation at P_3 is $T_{\text{meas}} \approx 49.5$, which compares favorably with the period $T_{\text{linear}} = 2\pi/\sqrt{\mathscr{U}_\beta \mathscr{V}_\beta} \approx 48.9$ predicted by the linear Hopf threshold.

At $P_4(0.065, 0.16)$, the temporal mode is unstable ($\mathcal{T}_0 < 0$), and the spatial mode $h = 2$ is also unstable ($\mathcal{R}_2 < 0$); the system thus exhibits a coexistence of spatial and temporal instabilities, and the resulting dynamics, shown in Figure 2(VII),(VIII), display a complex oscillatory pattern that is neither a pure Hopf limit cycle nor a purely spatial pattern, with a measured temporal period exhibiting fluctuations around $T_{\text{meas}} \approx 51.2$. To verify the long-time behavior, we extended the integration to $T = 2000$ and applied small random perturbations (amplitude 10^{-4}) at $t = 1000$. The solutions at P_3 returned to the same periodic orbit, suggesting local attractiveness, while those at P_4 remained in the complex oscillatory regime. Because a single perturbation test does not establish true orbital stability, a rigorous Floquet analysis or quantitative orbit-distance test is left for future work, and we carefully restrict our phrasing to a descriptive numerical characterization rather than claiming strict mathematical stability for these periodic solutions.

The stability region and bifurcation diagram of system (1.1) (linear Hopf threshold H_0 and Turing bifurcation lines L_h) are shown in Figure 1 with parameters $\alpha = 0.8$, $m = 0.5$, $c = 0.2$, $H = 0.1$, and $D_1 = 0.016$. Numerical simulations indicate that at $h = 2$, the slope of the L_h line reaches its maximum. In Figure 1(II), the points $P_1(0.06, 0.19)$, $P_2(0.07, 0.18)$, $P_3(0.065, 0.1638)$, $P_4(0.065, 0.16)$, and the intersection point $P(0.0655, 0.1684)$ between H_0 and L_2 are marked.

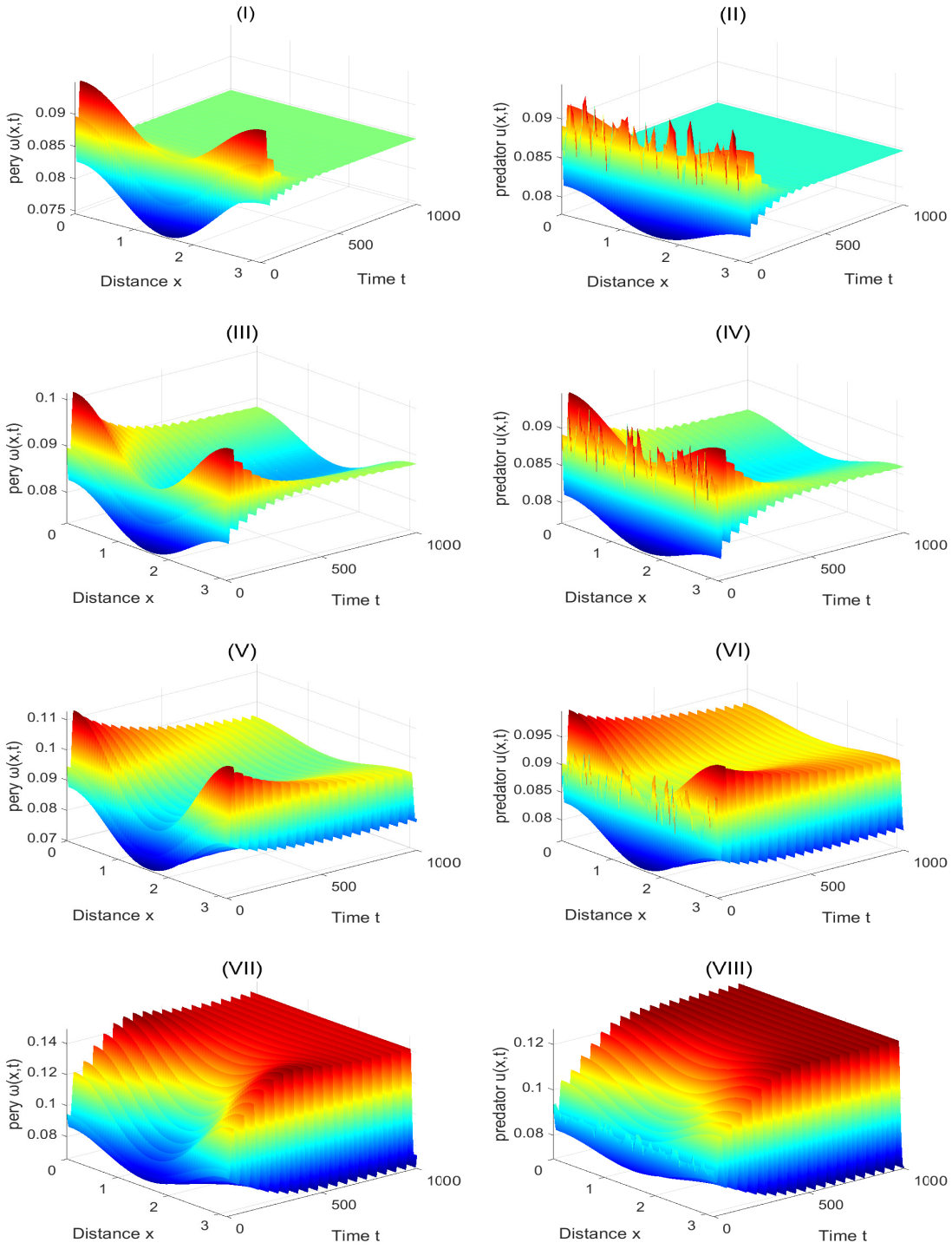

Figure 2. Space-time plots of prey density $\omega(x,t)$ and predator density $u(x,t)$ under different conditions with parameters $\alpha = 0.8$, $m = 0.5$, $c = 0.2$, $H = 0.1$, and $D_1 = 0.016$, for which the positive equilibrium is $E^* = (0.0847, 0.0847)$. I–II: P_1 (stable uniform steady state). III–IV: P_2 (long-lived transient spatial pattern with $\cos 2x$-like profile; the uniform state is linearly stable). V–VI: P_3 (numerically robust spatially inhomogeneous periodic solution with dominant $\cos 2x$ mode). VII–VIII: P_4 (spatially and temporally oscillatory pattern, with both homogeneous and spatial instabilities).

Remark 4.2. *The bifurcation conditions derived in Section 2 are given by explicit algebraic expressions, e.g., $\mathcal{R}_h = 0$ and $\mathcal{T}_h = 0$, in which the parameters enter polynomially or rationally. Consequently, the bifurcation boundaries are Lipschitz continuous with respect to small perturbations of the parameters, and no singular sensitivity occurs away from degeneracies. Near the intersection of the Turing bifurcation curve and the linear Hopf threshold, however, the spectral structure merits special attention: At such a generic intersection point, the spectrum consists of one simple zero eigenvalue (corresponding to the Turing mode) and one simple purely imaginary conjugate pair (corresponding to the linear Hopf mode), provided no additional multiplicity degeneracy occurs. In this region, small changes in the parameters can significantly alter the dynamical behavior, as observed in the numerical simulations at point P_3, where the system shifts from spatially inhomogeneous steady states to spatially inhomogeneous periodic oscillations. These numerical observations illustrate the rich interplay between spatial and temporal instabilities, but they do not constitute a rigorous codimension-two bifurcation analysis. A complete characterization of the nonlinear interaction at this point would require a normal-form computation, which is beyond the scope of the present paper and is left for future work.*

5. Conclusions

In this work, we have analyzed a diffusive predator–prey model that combines Smith growth, a ratio-dependent Holling type III functional response, and Leslie–Gower predator dynamics. Explicit conditions for Turing bifurcation and a linear stability threshold indicating the onset of Hopf-type oscillations were obtained in the (D_2, λ) parameter plane. For the Turing branch, we established the local existence of non-constant steady states bifurcating from the positive equilibrium. The stability of these bifurcating branches is not addressed analytically in this paper and is left for future investigation. Numerical simulations were then performed to complement these analytical results and to examine the system near the intersection of the Turing and Hopf curves. Instead of pure stationary patterns or pure homogeneous limit cycles, we observed long-lived transient spatial patterns, spatially inhomogeneous periodic solutions, and complex spatio-temporal instabilities.

Ecologically, the interplay between Turing and Hopf mechanisms marks a transition between temporal oscillations and spatial pattern formation. In the Turing-stable but weakly damped regime, slowly decaying prey–predator patches emerge, functioning as temporary refuges before returning to equilibrium. Near the intersection of the two bifurcation curves, the system exhibits spatially inhomogeneous periodic solutions, in which the prey and predator densities oscillate in time with a nontrivial spatial profile. In contrast, when both temporal and spatial modes are unstable, the system exhibits complex spatio-temporal oscillatory patterns. Thus, modest changes in λ or D_2 near the bifurcation point can move the system between qualitatively distinct dynamical regimes—a finding that underscores the sensitivity of spatial population dynamics to dispersal and demographic parameters.

Several points should be borne in mind regarding the scope of this work. The spatially inhomogeneous periodic solutions observed near the Turing–Hopf intersection are obtained numerically; a rigorous proof would require center manifold reduction and normal-form computation near the codimension-two point, which we have not attempted here. The analytical bifurcation result obtained here is restricted to the simple eigenvalue case. A complete treatment of multiple eigenvalue

interactions would require additional center-manifold or Lyapunov–Schmidt analysis. Moreover, although the model is motivated by ecological systems such as zooplankton–phytoplankton and forest–pest communities, direct comparisons with field data are not yet available; parameter estimation and empirical testing would be necessary before applying the theoretical predictions in practice.

Overall, the present study offers a mathematical framework for understanding how nonlinear growth, ratio-dependent predation, and spatial diffusion jointly influence the dynamics of this predator–prey system. The bifurcation conditions derived here may serve as a point of departure for further theoretical developments, including extensions to higher-dimensional domains, more general boundary conditions, and a full codimension-two analysis at the Turing–Hopf intersection.

Use of AI tools declaration

The authors declare they have not used Artificial Intelligence (AI) tools in the creation of this article.

Acknowledgments

This work was supported by the National Natural Science Foundation of China (Nos. 12361037, 12326357, 12326354, and 12361104), the Youth Talent Program of Xingdian Talent Support Plan (XDYC-QNRC2022-0514), the Yunnan Fundamental Research Projects (Nos. 202301AT070470, 202301AT070016, 202401AT070036, and 202601AS070071), the Special Project for Interdisciplinary Research of Kunming University of Science and Technology (ZZ2026XJ016A), the Yunnan Province Key Laboratory of Digital-Intelligent Ethnic Computing (Grant No. 20254916CE340003), and the Research on the Interdisciplinary Path between the Study of the Chinese Nation Community and Natural Science Disciplines (No. 2025GTT07).

Conflict of interest

The authors declare there are no conflicts of interest.

Data availability

The data that support the findings of this study are available from the corresponding author upon reasonable request.

References

1. F. E. Smith, Population dynamics in Daphnia magna and a new model for population growth, *Ecology*, **44** (1963), 651–663. https://doi.org/10.2307/1933011
2. H. Jiang, H. Fang, Y. Wu, Hopf bifurcation in a diffusive predator–prey model with Smith growth rate and herd behavior, *Adv. Differ. Equations*, **2020** (2020), 518. https://doi.org/10.1186/s13662-020-02879-4

3. W. Ding, W. Huang, Global dynamics of a ratio-dependent Holling–Tanner predator–prey system, *J. Math. Anal. Appl.*, **460** (2018), 458–475. https://doi.org/10.1016/j.jmaa.2017.11.057

4. P. H. Leslie, J. C. Gower, The properties of a stochastic model for the predator–prey type of interaction between two species, *Biometrika*, **47** (1960), 219–234. https://doi.org/10.1093/biomet/47.3-4.219

5. X. Fu, H. Jiang, Turing–Hopf bifurcation in a diffusive predator–prey model with schooling behavior and Smith growth, *Appl. Math. Lett.*, **159** (2025), 109257. https://doi.org/10.1016/j.aml.2024.109257

6. L. Li, X. P. Yan, C. H. Zhang, Turing, Hopf and Turing–Hopf bifurcations in a modified Leslie–Gower predator–prey diffusive system with Smith prey growth and nonmonotonic functional response, *Chaos, Solitons Fractals*, **201** (2025), 117226. https://doi.org/10.1016/j.chaos.2025.117226

7. W. J. Li, L. T. Zhang, J. D. Cao, A note on Turing–Hopf bifurcation in a diffusive Leslie–Gower model with weak Allee effect on prey and fear effect on predator, *Appl. Math. Lett.*, **172** (2026), 109741. https://doi.org/10.1016/j.aml.2025.109741

8. J. J. Wang, Y. F. Jia, M. J. Shi, Existence and Turing instability of positive solutions for a predator–pest model with additional food, *Appl. Math. Lett.*, **157** (2024), 109191. https://doi.org/10.1016/j.aml.2024.109191

9. C. R. Zhang, A. Ke, B. D. Zheng, Patterns of interaction of coupled reaction–diffusion systems of the FitzHugh–Nagumo type, *Nonlinear Dyn.*, **97** (2019), 1451–1476. https://doi.org/10.1007/s11071-019-05065-8

10. J. Li, Y. T. Ding, W. H. Jiang, Dynamical analysis of a pine wilt disease model with memory-based diffusion and nonlocal effect, *J. Math. Biol.*, **91** (2025), 6. https://doi.org/10.1007/s00285-025-02236-7

11. X. X. Ding, H. Shen, Y. L. Song, Spatial movement with explicit memory and nonlocal pregnancy delay, *Stud. Appl. Math.*, **154** (2025), e70011. https://doi.org/10.1111/sapm.70011

12. Z. H. Zhao, Y. W. Shen, Dynamic complexity of Holling–Tanner predator–prey system with predator cannibalism, *Math. Comput. Simul.*, **232** (2025), 227–244. https://doi.org/10.1016/j.matcom.2024.12.025

13. M. X. Chen, C. Tian, S. Ham, H. Kim, J. Kim, Impact of prey-taxis on a harvested intraguild predation predator–prey model, *Eur. J. Appl. Math.*, **36** (2025), 1183–1220. https://doi.org/10.1017/s0956792525000087

14. S. Ham, S. Kwak, A. Yun, Jyoti, Y. Nam, H. Kim, J. Kim, Traveling wave solutions for a normalized time-fractional predator–prey model, *Indian J. Phys.*, **100** (2026), 3357–3368. https://doi.org/10.1007/s12648-026-04021-8

15. X. W. Tan, J. H. Li, W. J. Li, X. Z. Liu, Dynamic analysis of diffusion dysentery diarrhoea epidemic model, *Commun. Nonlinear Sci. Numer. Simul.*, **152** (2026), 109245. https://doi.org/10.1016/j.cnsns.2025.109245

16. W. J. Li, W. H. Bai, J. D. Cao, Turing instability and pattern formation in a diffusive predator-prey system with opportunistic predators and weak Allee effect, *Phys. Rev. E*, **113** (2026), 044219. https://doi.org/10.1103/5fx7-q41y

17. W. J. Li, Y. Zhang, Q. Ding, J. S. Yu, Exponential convergence of a diffusive SIRS epidemic model with standard incidence, *J. Geom. Anal.*, **36** (2026), 13. https://doi.org/10.1007/s12220-025-02251-6

18. M. X. Chen, S. Ham, Y. Choi, H. Kim, J. Kim, Pattern dynamics of a harvested predator–prey model, *Chaos, Solitons Fractals*, **176** (2023), 114153. https://doi.org/10.1016/j.chaos.2023.114153

19. J. Zhou, Bifurcation analysis of a diffusive predator–prey model with ratio-dependent Holling type III functional response, *Nonlinear Dyn.*, **81** (2015), 1535–1552. https://doi.org/10.1007/s11071-015-2088-z

20. C. S. Holling, The functional response of predators to prey density and its role in mimicry and population regulation, *Mem. Entomol. Soc. Can.*, **97** (1965), 5–60. https://doi.org/10.4039/entm9745fv

21. M. Sivakumar, M. Sambath, K. Balachandran, Stability and Hopf bifurcation analysis of a diffusive predator–prey model with Smith growth, *Int. J. Biomath.*, **8** (2015), 1550013. https://doi.org/10.1142/s1793524515500138

22. S. Biswas, L. T. Bhutia, T. K. Kar, B. Bhunia, E. Das, Spatiotemporal analysis of a modified Leslie–Gower model with cross-diffusion and harvesting, *Physica D*, **470** (2024), 134381. https://doi.org/10.1016/j.physd.2024.134381

23. M. G. Crandall, P. H. Rabinowitz, Bifurcation from simple eigenvalues, *J. Funct. Anal.*, **8** (1971), 321–340. https://doi.org/10.1016/0022-1236(71)90015-2

AIMS Press